Materials Research Proceedings 28 (2023) 179-188 https://doi.org/10.21741/9781644902479-20

Analysis of additively manufactured anisotropic microstructures through crystal plasticity frameworks

BULUT Orhun[1,a], GÜNAY Enes[1,b] , FENERCIOĞLU Tevfik Ozan[2,c] and YALÇINKAYA Tuncay[1,d *]

[1]Department of Aerospace Engineering, Middle East Technical University, Ankara 06800, Türkiye

[2]Repkon Machine and Tool Industry and Trade Inc., 34980 Sile, Istanbul, Türkiye

[a]orhun.bulut@metu.edu.tr, [b]enes.gunay@metu.edu.tr, [c]ozan.fenercioglu@repkon.com.tr, [d]yalcinka@metu.edu.tr

Keywords: Crystal Plasticity, Size Effect, Additive Manufacturing

Abstract. In additive manufacturing processes, the resulting products might have highly anisotropic granular morphologies due to the complex thermal history. The most commonly observed morphology is columnar structure. The resulting morphology of grains is accompanied by the orientation alignment leading to plastic anisotropy. It has been shown in a recent study through local crystal plasticity calculations that the morphology evolution does not influence the mechanical behavior without considering the texture evolution [1]. However, the local frameworks do not consider the effect of the grain size which could be complicated due to high aspect ratio of the grains. This study aims to investigate the influence of the developed anisotropic grain structure on the macroscopic response through both local and non-local crystal plasticity frameworks to address the capacity of these models in capturing the realistic response. An additional subroutine is implemented (see [2]) into the crystal plasticity frameworks to obtain the slip resistance values at each material point based on grain geometries and misorientations. This allows the size dependent yielding of the crystals.

Introduction

Additively manufactured (AM) metallic alloy parts offer many benefits. The usage of additive manufacturing technology to create complex products has shown significant promise (see e.g. [3-6]). Through empirical studies over almost three decades, developments in additive manufacturing techniques have made them utilized in many industrial areas such as aerospace, automotive, construction. In these last decades, AM technology has become an important manufacturing methodology rather than a prototype production method. However, its application for manufacturing critical components is restricted by the inherent uncertainty associated with qualities, which frequently results from the variability in the manufacturing process itself (see e.g. [7]).

Some of the recent AM methods are based on melting and solidification of metallic powders during the process. Different kinds of microstructures can be resulted due to the complex thermal history of these processes which involve high temperature gradients and also high heating-cooling rates. This thermal history is highly dependent on the process parameters such as scanning strategy, hatch spacing, scan velocity. The high cooling rate in the complex heat transfer course during the AM processes results in the directional growth of grains. The thermal history influences not only the grain structure but also the grain orientation substantially (see [8]). Grain growth occurs along the direction of the highest temperature gradient where the solidification develops (see e.g. [9,10]). As a result, the final microstructures of AM products are observed to have anisotropic morphologies and consequent textures (see e.g. [11-13]). When additively made products are

examined, it becomes clear that crystal orientation alignment frequently occurs concurrently with the development of columnar grain structure (see e.g. [14-16]). Also, a common defect in AM products is their porous microstructure (see e.g. [17,18]). However, porosity is not examined in this study in order to solely focus on the grain and orientation alignment.

Additively manufactured parts show altered microstructures and mechanical properties with respect to the process parameters. Therefore, analyzing microstructures has importance for not only estimating their characteristics but also for adjusting the process parameters to achieve desirable mechanical properties.

In a previous study, the mechanical properties of microstructures consisting of elongated grain morphology are investigated through a rate dependent local crystal plasticity finite element framework (see [1]). In this paper, different crystal plasticity mechanisms are employed through different ABAQUS UMAT subroutines. First, simulations are conducted with only the local crystal plasticity framework. Then, a lower-order strain gradient crystal plasticity is implemented where, the impact of intrinsic size effects is addressed. A higher-order strain gradient formulation could also have been used as in [19,20] through a UEL, however it is omitted in the current study. A lower-order approach can be a good starting point for comparing different crystal plasticity mechanisms.

Along with the implementation of lower-order strain gradient crystal plasticity, a different mechanism is also studied to recalculate the initial slip resistance of each material point as in [2]. With this method, the slip resistance of each slip system for every material point is calculated considering grain orientations and the distance of points to grain boundaries.

The structure of this work is as follows. Firstly, the crystal plasticity frameworks used in the finite element simulations are described. Then, the method for determining model parameters and producing polycrystalline representative volume elements (RVEs) is provided. Orientation restrictions on the grains to obtain a more realistic grain alignment are given. Finally, the outcomes of crystal plasticity finite element method (CPFEM) simulations are shown and thoroughly explained for the three methods used.

Crystal Plasticity Frameworks

In the current study, first, a local finite strain rate-dependent crystal plasticity framework (see [21]) is adapted for the analyses of microstructures (see [22,23] for example applications of this framework). In this framework, the deformation gradient $\boldsymbol{F}$ is multiplicatively decomposed into elastic part $\boldsymbol{F}^e$ and plastic part $\boldsymbol{F}^p$**.** Plastic velocity gradient can be obtained by integrating the plastic slip rates $\dot{\gamma}$ overall slip systems as

$$\mathbf{L}^{\mathrm{p}}=\dot{\mathbf{F}}^{\mathrm{p}}\mathbf{F}^{\mathrm{p}-1}=\sum_{\alpha=1}^{\mathrm{N}}\dot{\gamma}^{\alpha}\,(\mathbf{m}^{\alpha}\otimes\mathbf{n}^{\alpha}) \tag{1}$$

where α defines the slip system. $\boldsymbol{m}^{\boldsymbol{\alpha}}$ and $\boldsymbol{n}^{\boldsymbol{\alpha}}$ are the slip direction and slip normal of the slip system respectively. In this work, an aluminum alloy is analyzed with all 12 slip systems of the face-centered cubic (FCC) crystal. All slip systems are active at all times, since a rate-dependent model is used. The slip rate of the slip systems $\dot{\gamma}^{\alpha}$ is governed by the power law

$$\dot{\gamma}^{\alpha}=\dot{\gamma}_0=\left|\frac{\tau^{\alpha}}{g^{\alpha}}\right|^{n} sign(\tau^{\alpha}) \tag{2}$$

where $\dot{\gamma}_0$ is the reference slip rate, τ^{α} is the resolved shear stress, g^{α} is the slip resistance and n is the rate sensitivity exponent. The slip resistance consists of statistically stored dislocations (SSDs) and geometrically necessary dislocations (GNDs) parts.

$$g^{\alpha} = \sqrt{{g^{\alpha}_{ssd}}^{2} + {g^{\alpha}_{gnd}}^{2}} \tag{3}$$

For local crystal plasticity simulations, only the hardening from SSDs is considered, which is described by the following relation,

$$\dot{g}^{\alpha}_{ssd} = \sum_{\beta=1}^{N} h^{\alpha\beta} \left|\dot{\gamma}^{\beta}\right| \tag{4}$$

where N represents the number of total slip systems and latent hardening is $h^{\alpha\beta} = q^{\alpha\beta} h^{\alpha\alpha}$, where $q^{\alpha\beta}$ is the latent hardening coefficient. Peirce and Asaro's (sech) self-hardening law is used for the self-hardening,

$$h^{\alpha\alpha} = h_0 \left|\frac{h_0 \gamma}{g_s - g_0}\right|, \tag{5}$$

where h_0 is the initial hardening modulus, g_0 is the initial slip resistance and g_s is the saturation slip resistance. The implementation of a lower-order strain gradient framework into the crystal plasticity subroutine enables the inclusion of additional hardening as a result of GNDs. This implementation allows an intrinsic length scale parameter to be defined and the size effects to be captured [24].

$$g^{\alpha}_{gnd} = g_0 \sqrt{l \eta^{\alpha}_{gnd}} \tag{6}$$

where $l = \frac{\alpha_T^2 \mu_s^2 b}{g_0^2}$ is the length scale parameter, α_T is the Taylor coefficient, μ_s is the shear modulus and b is the length of Burger's vector. Density of GNDs on a slip system α is defined as,

$$\eta^{\alpha}_{gnd} = \left|\mathbf{n}^{\alpha} \times \sum_{\beta=1}^{N} \mathbf{m}^{\alpha} \mathbf{m}^{\beta} \nabla \gamma^{\beta} \times \mathbf{n}^{\beta}\right| \tag{7}$$

Numerical Analysis

All the crystal plasticity simulations are conducted with the commercial finite element analysis software ABAQUS using brick (C3D8) elements. The material used in all finite element method (FEM) simulations is AA6016 in T4 condition. The hardening parameters are fitted in a previous study (see [1]). The hardening parameters are taken as initial hardening modulus $h_0 = 190\ MPa$, saturation slip resistance $g_s = 95\ MPa$ and initial slip resistance $g_0 = 47 MPa$. Cubic elastic coefficients for aluminum sheet are used as $C_{11} = 108.2\ GPa$, $C_{12} = 61.3\ GPa$, and $C_{44} = 28.5\ GPa$ [25]. Reference slip rate $\dot{\gamma}_0$ is taken as $10^{-3}\ s^{-1}$ and rate sensitivity parameter n is taken as 20. A strong latent hardening is assumed for aluminum and q is taken as 1.4. To observe the strain gradient effects clearly, the length scale parameter is taken as 500 μm in non-local strain gradient CPFEM simulations.

The user subroutine code (UMAT) based on [21] is modified to recalculate the initial slip resistance g_0. This modification will be referred as geometry-dependent slip resistance subroutine in the consecutive sections. With this subroutine, initial slip resistance is calculated by the distance of material points to grain boundaries and grain orientations. This theory aims to simulate the influence of dislocation piling up at grain boundaries. The details can be found in [2]. The aim of this method is to examine size effects based on Hall-Petch relation. Initial slip resistance is calculated as,

$$g_0^\alpha = \tau_0 + \frac{K\left(1-m^{\alpha'}\right)^c}{\sqrt{L^\alpha}} \quad (8)$$

τ_0 is taken as the critically resolved shear stress of a theoretically infinite crystal which is considered as zero. This value is taken as close to zero, which is 0.05 MPa. L^α is the distance of a material point to grain boundaries in the slip direction. K and c are empirical coefficients taken as 0.414 and 0.134. Their values are obtained by fitting the stress-strain curve of 300 grain RVE with 47 MPa initial slip resistance. $m^{\alpha'}$ is the Luster-Morris parameter for each slip system and is found from the misorientations of grains as $m^{\alpha'} = \left(\frac{\boldsymbol{m}_A^\alpha . \boldsymbol{m}_B^\alpha}{|\boldsymbol{m}_A^\alpha||\boldsymbol{m}_B^\alpha|}\right)\left(\frac{\boldsymbol{n}_A^\alpha . \boldsymbol{n}_B^\alpha}{|\boldsymbol{n}_A^\alpha||\boldsymbol{n}_B^\alpha|}\right)$ where $\boldsymbol{m}^\alpha$ and $\boldsymbol{n}^\alpha$ are slip direction and slip normal respectively. Subscripts A and B correspond grains A and B respectively.

Polycrystalline RVEs with 300 grains are generated through Voronoi Tessellation (see [26]). Each morphology represents different grain elongation levels and is named as Equiaxed, Needle1, Needle2, Needle3 in consecutive parts of the paper. Grain aspect ratios are (1,1,1), (0.5,1,0.5), (0.25,1,0.25) and (0.1,1,0.1) for Equiaxed, Needle1, Needle2, Needle3 respectively. Grain morphologies can be seen in Fig. 1.

10% displacement is given to RVEs as the loading condition with $10^{-3}\ s^{-1}$ strain rate. Boundary conditions are applied such that all surfaces are kept straight and it is ensured that the stress triaxiality value stays constant at 0.33 during the loading (see e.g. [27]).

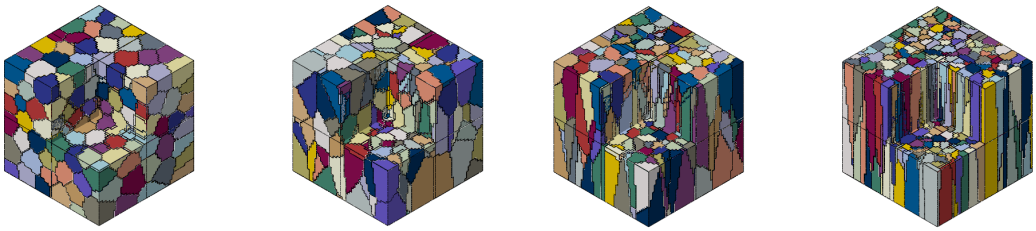

Fig. 1. Polycrystal RVE morphologies, from left to right: Equiaxed, Needle1, Needle2, Needle3.

Initially, all the RVEs are simulated at the same set of random orientations with the aforementioned crystal plasticity mechanisms separately. Following ZYX Euler convention, different orientation angle restrictions are assigned to corresponding RVEs. Crystals are tilted around the building direction (Y-axis) by restricting the X and Z rotations while the Y rotation is kept at zero. For restricted cases, [-90 +90], [-30 +30], [-10 +10] restricted intervals are assigned to Needle1, Needle2, Needle3 respectively. No restriction is applied for random orientation cases.

Numerical Results

Firstly, only the effects of grain morphologies are compared. All RVEs are assigned grains with the same set of random crystal orientations. A series of crystal plasticity finite element analyses using the three aforementioned mechanisms (i.e. local, strain-gradient, and geometry-dependent initial slip resistance subroutine in the local framework) are performed on every morphology by applying 10% strain in building-direction (Y axis) and the normal direction (Z axis) separately.

When there are no orientation restrictions on the grains (i.e., each one is randomly oriented), all three methods give very similar stress vs. strain responses. In Fig. 2a and Fig 2b, the results under the non-local crystal plasticity and geometry-dependent initial slip resistance modification are shown. Due to the presence of additional slip resistance from GND densities in the framework, higher amount of hardening with respect to the local framework is observed. However, beyond that, isotropic response is obtained for randomly oriented RVEs with all three methods.

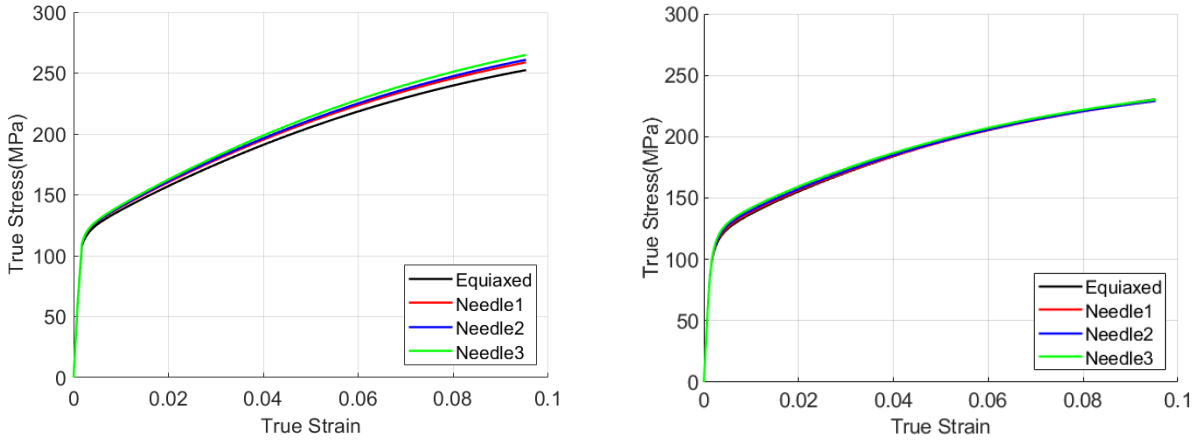

a) Non-local, building direction *b) Modified , building direction*

Fig. 2. Stress vs. Strain response of RVE finite element simulations with randomly oriented grains using different frameworks.

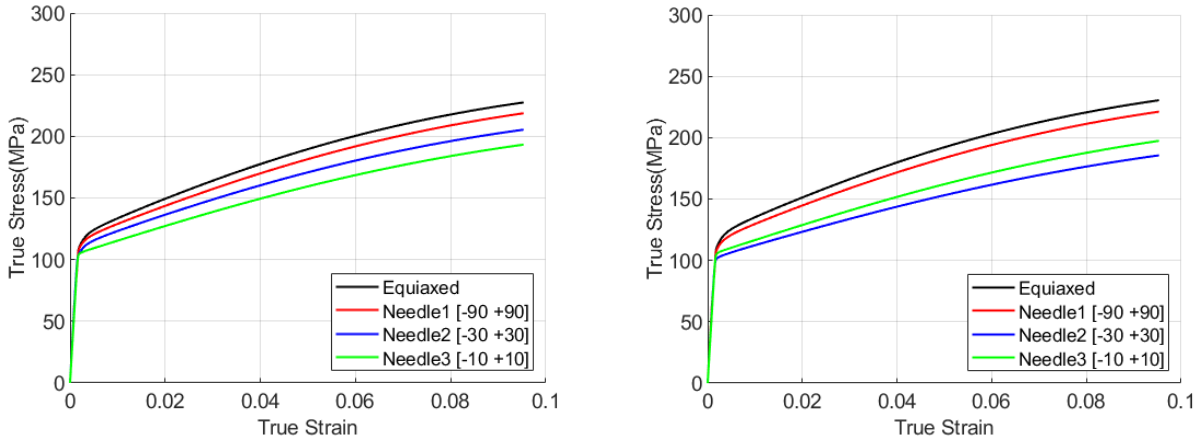

a) Building direction *b) Normal direction*

Fig. 3. Stress vs. Strain response of RVE finite element simulations with restricted crystal orientations using local framework with loading in building and normal directions.

To examine the results in a more realistic case, the crystal orientations of the grains have been increasingly aligned with the loading direction as the aspect ratio increases. The orientations of equiaxed grain morphology have been kept unrestricted. The rotations of crystals in X and Z axes have been restricted to previously mentioned intervals of Euler angles and the results are presented in Fig. 3. When the grains become more aligned, misorientations start to diminish gradually. Analyses in local framework have shown that, rather than the morphology, orientation has more impact on the mechanical response. A more anisotropic response is obtained for Needle2 case with [-30 +30] restriction compared to Needle1 and Equiaxed when the responses are compared in building and normal direction loading cases. However, the extreme case RVE with Needle3 morphology and [-10 +10] angle restriction does not show significant anisotropic response. This is because the misorientations between the grains are so small that it behaves as if there is a crystal symmetry between the grains.

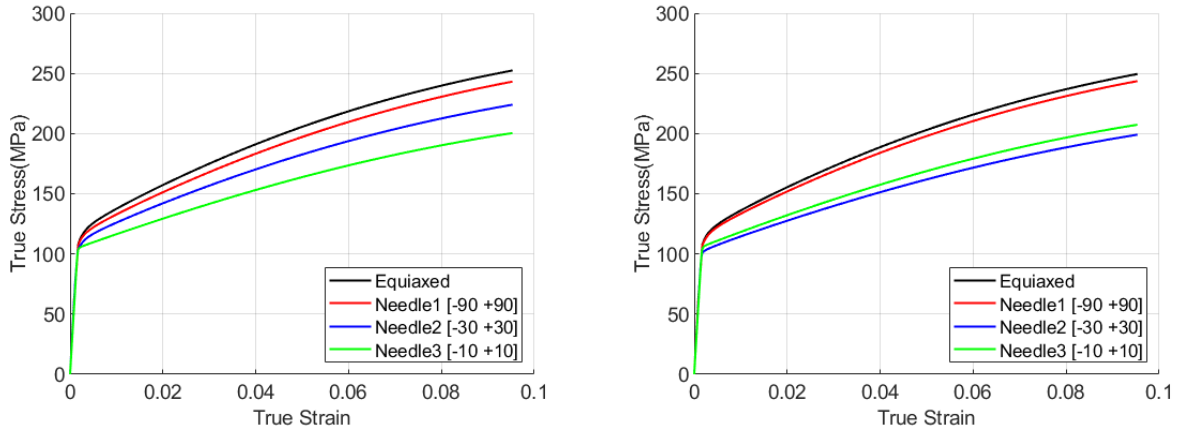

a) Building direction *b) Normal direction*

Fig. 4. Stress vs. Strain response of RVE finite element simulations with restricted crystal orientations using non-local framework with loading in building and normal directions.

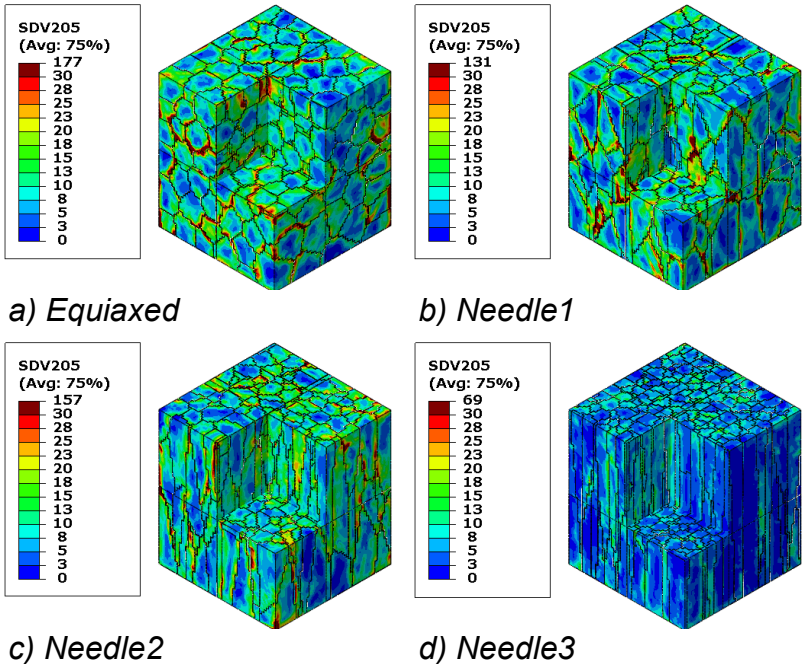

Fig. 5. Distribution of GND densities [1/mm] in RVEs from strain gradient framework simulations after loading in building direction with restricted orientations.

Fig. 4 shows the results of the same simulations through the strain gradient crystal plasticity framework. Needle2 shows highly anisotropic behavior compared to other morphologies similar to local framework. General trend of decrease in stress results stays same as the orientations become more restricted. However, there is an increased gap between the stress response of RVEs. This is a result of reduced misalignment between the grains causing GND densities to exist in smaller quantities. This can be seen in Fig. 5 as well, where the distributions of GND densities of all morphologies are shown. GNDs are most prominent at the grain boundaries. As the grains become more oriented in a particular direction (in this case, the building direction), the density of GNDs and their contribution to hardening begin to decrease.

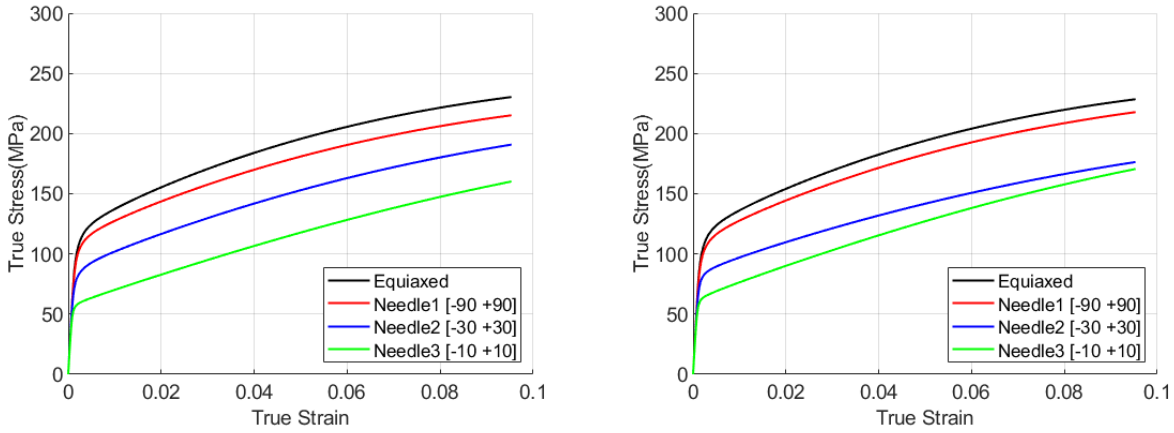

a) Building direction *b) Normal direction*

Fig. 6. Stress vs. Strain response of RVE finite element simulations with restricted crystal orientations using modified after loading in building and normal directions.

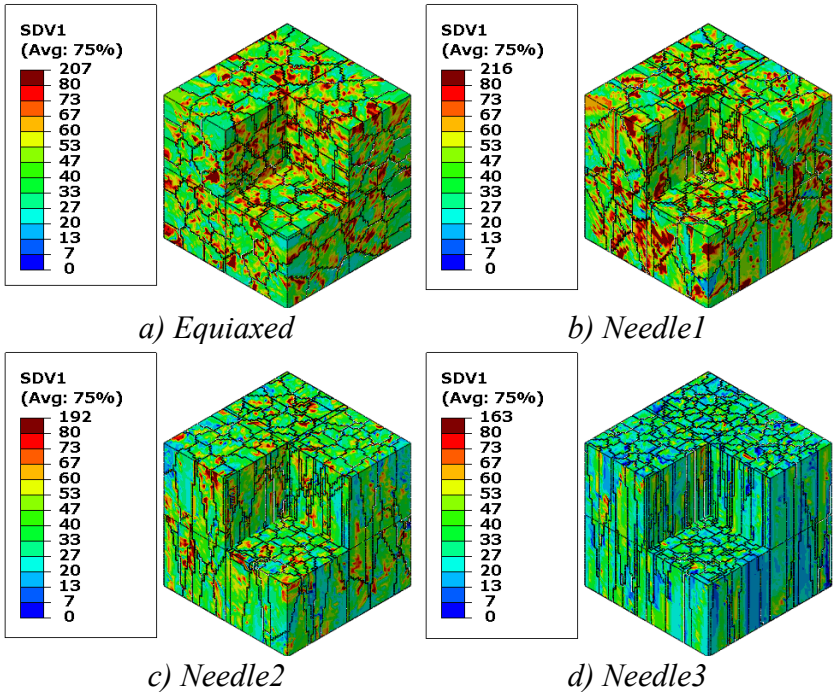

a) Equiaxed *b) Needle1*

c) Needle2 *d) Needle3*

Fig. 7. Distribution of the modified initial slip resistance g_0 in RVEs with restricted orientations.

The stress vs. strain results of simulations using the geometry-dependent initial slip resistance calculation subroutine are shown in Fig. 6. The most important factor here is that both of the previous methods do not affect the yielding point of the material significantly. This is because the initial slip resistance of the material is taken as constant. However, when the influence of morphology and orientation on the initial slip resistance is taken into account, overall yielding points of the RVEs also differ. As the grain orientations become more aligned, the yield stress of the RVE decreases as a result. In Fig 6b, it can be seen that stress values of Needle2 and Needle3 become closer when they are loaded in normal direction as opposed to building direction. This is a result of modifying the initial slip resistance. In both previously examined methods (i.e. local and non-local cases), Needle3 shows a higher stress response for normal direction loading. However, modifying the g_0 decreases the yield point so much that the stress value of Needle3

becomes lower than that of Needle2 at the end of displacement. This is a different result compared to ones obtained with other frameworks, since Needle2 shows the weakest response in normal direction in both local and non-local methods. Similar in other methods, anisotropic behavior is the strongest in Needle2.

The distribution of initial slip resistance calculated from the grain geometries and orientations are shown in Fig. 7. The randomly oriented Equiaxed morphology and the [-90 +90] restricted Needle1 morphology shows a similar distribution. This is also seen in Fig. 7 from their yield stress distributions being similar. On the other hand, when the misorientation between grains decreases in Needle2 and Needle3, there are fewer points with high initial slip resistance.

Summary

In this paper, anisotropic granular morphologies which developed in additive manufacturing techniques are examined with different crystal plasticity frameworks. Grains are elongated step by step for different RVEs.

Firstly, only the effect of morphology is examined with different crystal plasticity frameworks. It has been observed that when the strain gradient framework is taken into account, morphology without providing the proper texture does not significantly change the outcomes as in the prior study [1]. However, using a non-local model has benefits in terms of locating the GND density accumulations, especially at the grain boundaries. The influence of texture on GND densities is discussed and results have proven that lower-order SGCP can be a useful framework for the recognition of dislocation pile-ups in additive manufacturing products.

Different stress responses are obtained for different loading directions when grain orientations are restricted. Even though the lower-order SGCP framework contributes to hardening and makes stress responses stronger, it does not change the general trend observed in the previous study. In Needle1's case, a large range of possible orientations does not yield an anisotropic response regardless of the framework used in simulations. Needle2, on the other hand, shows a highly anisotropic response from the results with all frameworks since orientation restrictions on the grains is much narrower compared to Needle1. While Needle3 is assigned with most narrow orientation restrictions, the material shows less anisotropic behavior than Needle2. This is a result of building and normal directions lying on the symmetry axes of FCC crystal. Heavily aligning all grains with the loading direction causes the material to act similar to a single crystal specimen since grain misorientations become small. Without a modification of the initial slip resistance of grains, Needle3 displays a stronger response compared to Needle2 in normal direction. However, by modifying its initial slip resistance based on grain geometries and orientations, the yield stress of Needle3 is predicted to be lower than all other morphologies in normal direction.

References

[1] S.S. Acar, O. Bulut, T. Yalçinkaya, Crystal plasticity modeling of additively manufactured metallic microstructures, Procedia Struct. Integrity 35 (2022) 219-227. https://doi.org/10.1016/j.prostr.2021.12.068

[2] D. Agius, A. Kareer, A. Al Mamun, C. Truman, D.M. Collins, M. Mostafavi, D. Knowles, A crystal plasticity model that accounts for grain size effects and slip system interactions on the deformation of austenitic stainless steels, Int. J. Plast. 152 (2022) 103249. https://doi.org/10.1016/j.ijplas.2022.103249

[3] F. Singer, D. Deisenroth, D. Hymas, M. Ohadi, Additively manufactured copper components and composite structures for thermal management applications, in: 2017 16th IEEE Intersociety Conference on Thermal and Thermomechanical Phenomena in Electronic Systems (ITherm), IEEE, 2017: pp. 174-183. https://doi.org/10.1109/ITHERM.2017.7992469

[4] M. Lowther, S. Louth, A. Davey, A. Hussain, P. Ginestra, L. Carter, N. Eisenstein, L. Grover, S. Cox, Clinical, industrial, and research perspectives on powder bed fusion additively

manufactured metal implants, Addit. Manuf. 28 (2019) 565-584. https://doi.org/10.1016/j.addma.2019.05.033
[5] B. Blakey-Milner, P. Gradl, G. Snedden, M. Brooks, J. Pitot, E. Lopez, M. Leary, F. Berto, A. du Plessis, Metal additive manufacturing in aerospace: A review, Mater. Des. 209 (2021) 110008. https://doi.org/10.1016/j.matdes.2021.110008
[6] A. Uriondo, M. Esperon-Miguez, S. Perinpanayagam, The present and future of additive manufacturing in the aerospace sector: A review of important aspects, Proc. Inst. Mech. Eng., Part G: J. Aerosp. Eng. 229 (2015) 2132-2147. https://doi.org/10.1177/095441001456879
[7] J.C. Najmon, S. Raeisi, A. Tovar, Review of additive manufacturing technologies and applications in the aerospace industry, Additive Manufacturing for the Aerospace Industry. (2019) 7-31. https://doi.org/10.1016/B978-0-12-814062-8.00002-9
[8] T.F. van Nuland, J. van Dommelen, M.G. Geers, Microstructural modeling of anisotropic plasticity in large scale additively manufactured 316L stainless steel, Mech. Mater. 153 (2021) 103664. https://doi.org/10.1016/j.mechmat.2020.103664
[9] Z. Wang, K. Guan, M. Gao, X. Li, X. Chen, X. Zeng, The microstructure and mechanical properties of deposited-IN718 by selective laser melting, J. Alloys Compd. 513 (2012) 518-523. https://doi.org/10.1016/j.jallcom.2011.10.107
[10] E.W. Hovig, A.S. Azar, F. Grytten, K. Sørby, E. Andreassen, Determination of anisotropic mechanical properties for materials processed by laser powder bed fusion, Adv. Mater. Sci. Eng. 2018 (2018). https://doi.org/10.1155/2018/7650303
[11] E. Yasa, J. Deckers, J.-P. Kruth, The investigation of the influence of laser re-melting on density, surface quality and microstructure of selective laser melting parts, Rapid Prototyping J. 17 (2011) 312-327. https://doi.org/10.1108/13552541111156450
[12] C. Qiu, N.J. Adkins, M.M. Attallah, Microstructure and tensile properties of selectively laser-melted and of HIPed laser-melted Ti–6Al–4V, Mater. Sci. Eng. A 578 (2013) 230-239. https://doi.org/10.1016/j.msea.2013.04.099
[13] B. Song, X. Zhao, S. Li, C. Han, Q. Wei, S. Wen, J. Liu, Y. Shi, Differences in microstructure and properties between selective laser melting and traditional manufacturing for fabrication of metal parts: A review, Front. Mech. Eng. 10 (2015) 111-125. https://doi.org/10.1007/s11465-015-0341-2
[14] A. Charmi, R. Falkenberg, L. Ávila, G. Mohr, K. Sommer, A. Ulbricht, M. Sprengel, R.S. Neumann, B. Skrotzki, A. Evans, Mechanical anisotropy of additively manufactured stainless steel 316L: An experimental and numerical study, Mater. Sci. Eng. A 799 (2021) 140154. https://doi.org/10.1016/j.msea.2020.140154
[15] A.A. Antonysamy, J. Meyer, P. Prangnell, Effect of build geometry on the β-grain structure and texture in additive manufacture of Ti6Al4V by selective electron beam melting, Mater. Charact. 84 (2013) 153-168. https://doi.org/10.1016/j.matchar.2013.07.012
[16] K. Hara, K. Itoh, M. Kamiya, H. Fujiwara, K. Okamoto, T. Hashimoto, Alignment of crystallites in obliquely deposited cobalt films, Jpn. J. Appl. Phys. 33 (1994) 3448. https://doi.org/10.1143/JJAP.33.3448
[17] K. Moussaoui, W. Rubio, M. Mousseigne, T. Sultan, F. Rezai, Effects of Selective Laser Melting additive manufacturing parameters of Inconel 718 on porosity, microstructure and mechanical properties, Mater. Sci. Eng. A 735 (2018) 182-190. https://doi.org/10.1016/j.msea.2018.08.037
[18] B. Zhang, S. Liu, Y.C. Shin, In-Process monitoring of porosity during laser additive manufacturing process, Addit. Manuf. 28 (2019) 497-505. https://doi.org/10.1016/j.addma.2019.05.030

[19] T. Yalçinkaya, Strain gradient crystal plasticity: Thermodynamics and implementation, in: G. Z. Voyiadjis (Eds.), Handbook of Nonlocal Continuum Mechanics for Materials and Structures, Springer, London/Berlin, 2017, pp.1001-1033.
[20] T. Yalçinkaya, İ. Özdemir, İ. Tarik Tandoğan, Misorientation and grain boundary orientation dependent grain boundary response in polycrystalline plasticity, Computational Mechanics. 67 (2021) 937-954. https://doi.org/10.1007/s00466-021-01972-z
[21] Y. Huang, A user-material subroutine incorporating single crystal plasticity in the ABAQUS finite element program, Mech. Report 178 (1991).
[22] O. Bulut, S. S. Acar, T. Yalçinkaya, The influence of thickness/grain size ratio in microforming through crystal plasticity, Procedia Struct. Integrity 35 (2022) 228-236. https://doi.org/10.1016/j.prostr.2021.12.069
[23] T. Yalçinkaya, B. Tatli, I.E. Ünsal, I.U. Aydiner, Crack Initiation and Propagation in Dual-phase Steels Through Crystal Plasticity and Cohesive Zone Frameworks, Proce. Struct. Integrity 42 (2022) 1651-1659.
[24] C. S. Han, H. Gao, Y. Huang, W. D. Nix, Mechanism-based strain gradient crystal plasticity—I, Theory, J. Mech. Phys. Solids 53 (2005) 1188-1203. https://doi.org/10.1016/j.jmps.2004.08.008
[25] E. Nakamachi, C. Xie, H. Morimoto, K. Morita, N. Yokoyama, Formability assessment of FCC aluminum alloy sheet by using elastic crystalline viscoplastic finite element analysis, Int. J. Plast. 18 (2002) 617-632. https://doi.org/10.1016/S0749-6419(01)00052-3
[26] R. Quey, P. Dawson, F. Barbe, Large-scale 3D random polycrystals for the finite element method: Generation, meshing and remeshing, Comput. Methods Appl. Mech. Eng. 200 (2011) 1729-1745. https://doi.org/10.1016/j.cma.2011.01.002
[27] T. Yalçinkaya, S.O. Çakmak, C. Tekoğlu, A crystal plasticity based finite element framework for RVE calculations of two-phase materials: Void nucleation in dual-phase steels, Finite Elem. Anal. Des. 187 (2021) 103510. https://doi.org/10.1016/j.finel.2020.103510